

SUPPLEMENTARY INFORMATION

Phase (trans)formation and physical state of a model drug in mesoscopic confinement

Tina Ukmar¹, Aljaž Godec¹, Odon Planinšek², Venčeslav Kaučič^{1,3}, Gregor Mali¹
and Miran Gaberšček^{1,3,*}

¹*National Institute of Chemistry, Hajdrihova 19, SI-1000 Ljubljana, Slovenia*

²*Faculty of Pharmacy, University of Ljubljana, Aškerčeva 7m, SI-1000 Ljubljana, Slovenia*

³*Faculty of Chemistry and Chemical Technology, Aškerčeva 5, SI-1000 Ljubljana, Slovenia*

S1: More details on Experimental procedures

Synthesis of SBA-15 matrix. Ordered mesoporous silicate (SBA-15) with an average pore size of 8.9 nm was prepared with a hydrothermal synthesis using the structure directing agent Pluronic P123 (PEG-PPG-PEG block copolymer, Aldrich) and tetraethyl orthosilicate (98 % TEOS, Aldrich) as a silica source with the $n_{\text{TEOS}}/n_{\text{P123}}$ ratio around 70. First, 3.4 g of Pluronic P123 was dissolved in a mixture of 120 g distilled water and 30 g hydrochloric acid (37 % HCl, Aldrich). This mixture was placed in an oil bath at 303 K under magnetic stirring. After 3 h of stirring, 8.5 g of TEOS was added dropwise to the Pluronic P123 solution and stirred at 313 K for 8 h. The stirring was continued at 348 K overnight. Then the silica suspension was transferred into a Teflon-lined autoclave and placed in an oven for hydrothermal treatment at 373 K for 24 h. The obtained white powder was washed on a filter with distilled water to a pH 6 – 6.5, dried at 298 K for 24 h and calcined at 823 K for 6 h in an air flow to remove the triblok copolymer from the pores.

Synthesis of MCM-41 matrix. Ordered mesoporous silicate (MCM-41) with a mean pore diameter of 3.5 nm was synthesized using the structure directing agent hexadecyltrimethylammonium bromide (CTAB, Aldrich) and tetraethyl orthosilicate (98 % TEOS, Aldrich) as a silica source. First, 1.7 ml of 2 M NaOH was added to 240 g of distilled water under stirring at room temperature. Then, 500 g of CTAB was added to the solution with stirring and heating from room temperature to 338 K. When the solution had become homogeneous, 2.5 g of TEOS was added dropwise. After 3 h of stirring and heating at 338 K, the obtained white powder was washed on a filter with distilled water to a pH 7, dried at 323 K for 24 h and calcined at 823 K for 6 h in an air flow to remove CTAB from the pores.

Drug loading procedures. First, a sub-saturated solution of indomethacin (γ -IMC, Sigma) was prepared in various solvents (tetrahydrofuran (THF), acetone and ethanol; Sigma-Aldrich). The sub-saturated solution was added dropwise to a fine layer of calcined samples

of SBA-15 and MCM-41, allowing the powder to soak the added drops. The prepared samples were then dried, first at 313 K for 24 h and then at 313 K in vacuum. Because of the high solubility of IMC in THF, THF was chosen as a loading solvent for further analysis. Calcined SBA-15 and MCM-41 were then loaded with increasing amounts of IMC solutions (IMC / THF: 25 mg /g, 37 mg/g, 50 mg/g, 75 mg/g, 100 mg/g and 190 mg/g) followed by a two-step drying process. Several drying strategies were employed as described in continuation.

Drying procedures

Several drying strategies were employed, including single step drying in a ventilation dryer, a vacuum dryer and a two step combination of both. It was found that the two step strategy, including drying at 40 °C for 24 h in a ventilation dryer followed by drying at 40 °C for 24 h in a vacuum dryer, gave the most reproducible results. The first step is supposed to remove the majority of the solvent, whereas the second step removes the residual solvent that is adsorbed more strongly to the pore walls or that is capillary condensed. Immediately after drying, the samples were placed in an exiccator under inert Ar atmosphere to avoid exposure to moisture and were kept in such conditions until immediately before the measurements. It was found that such pretreatment decisively enhanced the reproducibility while avoiding the otherwise very prominent effects of residual loading solvent and/or water.

Characterization

X-Ray Powder Diffraction (XRPD) and Thermodiffraction (XRPTD). X-ray powder diffraction (XRPD) patterns were recorded on a PANalytical X'Pert PRO high-resolution diffractometer with Alpha 1 configuration using CuK_{α1} radiation (1.5406 Å) in the range from 0.5 to 5 ° 2θ, using a step of 0.017 ° per 100 s and in the range from 5 to 35 ° 2θ, using a step of 0.033 ° per 100 s under air conditions. Structural changes of β-IMC during the heating were investigated on a PANalytical X'Pert PRO high-resolution thermodiffractometer with Alpha 1 configuration using CuK_{α1} radiation (1.5406 Å) in the range from 5 to 35 ° 2θ, using step of 0.039 ° per 100 s under N₂ conditions with heating rate of 5 K/min. Diffraction patterns were recorded in the range of phase transformation from β-IMC to α-IMC (358 K – 393 K) at different temperatures and at the melting temperature of α-IMC.

Helium pycnometric density (He-pycnometry) and calculation of Connolly densities.

Prior the analysis the pycnometer AccuPyc 1330 (Micromeritics, Norcross, GA) was calibrated against standard volume of two stainless steel balls. Each determination included five purges prior to analysis and three analytical runs. Each sample was analyzed in triplicate by accurate weighing of powder in the measurement cell. In an infinitely diluted phase (i.e. all molecules are completely isolated) the maximum possible density, which can be measured by

He-pycnometry (the excluded volume density of isolated molecules), corresponds to the Connolly volume of the phase with a certain composition. The Connolly volumes were estimated using molecular conformations obtained by vacuum energy minimization on the molecular mechanics MM2 level. The volumes were calculated by rolling a He atom (with van der Waals radius 2.11 Å) over the molecular surface (for details see Supplementary Information S6).

S2: X-ray powder diffraction (XRPD)

S2.1 XRPD analysis of IMC polymorphs

We analyzed the prepared crystalline polymorphs of IMC (α , β and γ) by means of XRPD. α -IMC was prepared by recrystallization of γ -IMC from ethanol. β -IMC, which is a pseudo-polymorph (a solvate with THF), was prepared by recrystallization of γ -IMC from THF. The diffraction patterns were in agreement with those reported in the literature¹⁻³, which confirmed that the recrystallization was successful (Fig. S2.A).

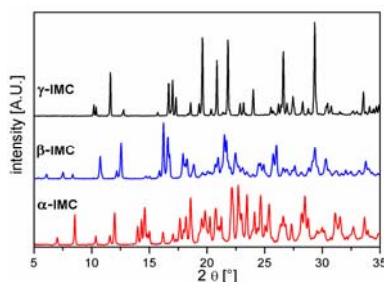


Fig. S2.A: XRPD patterns of prepared α , β and γ polymorphs of IMC.

S2.2 Ability of XRPD to detect IMC particles deposited inside and outside the pores

We investigated the properties of IMC-loaded samples. In the first set of experiments we loaded the silicates with solutions having increasing amounts of IMC in THF to probe the detectability of excess IMC deposited outside the pores by means of XRPD. Here we assumed that XRPD could not detect crystalline particles with sizes as small as the present pore size (3.5-9 nm) because the number of scattering centers in such small particles is too low to assure detectable constructive X-ray interference. Thus, it is expected that samples with incompletely filled pores will exhibit amorphous XRPD patterns, whereas the excess of IMC deposited outside the pores will give detectable peaks (Fig. S2.B).

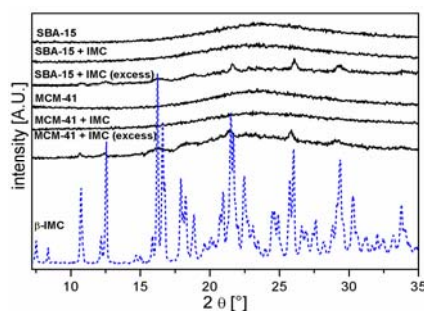


Fig. S2.B: XRPD patterns of SBA-15 (left) and MCM-41 (right) loaded with increasing amounts of subsaturated solution of IMC in THF.

After establishing that XRPD is able to detect IMC particles located outside the pores, we recorded XRPD patterns of samples used for further analysis.

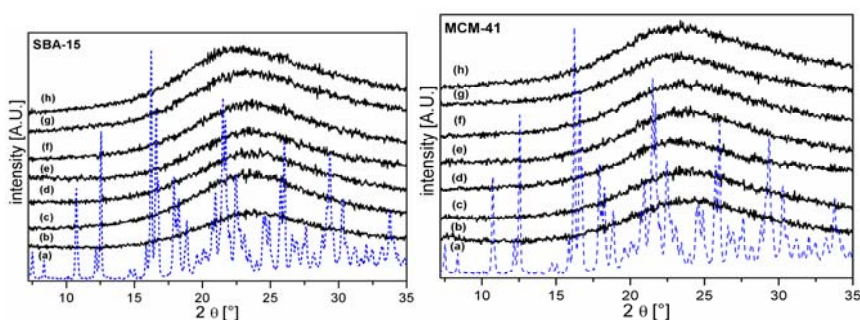


Fig. S2.C: XRPD patterns of SBA-15 (left) and MCM-41 (right) loaded with solution of IMC in THF with increasing concentrations.

The XRPD patterns are given in Figure S2.C. As seen, they contain no peaks corresponding to crystalline IMC, thus we may conclude that IMC is located solely inside the pores.

S2.3 Structural evolution of β-IMC during thermal treatment

To investigate the structural features of β-IMC during thermal treatment we recorded XRPD patterns at different temperatures (see Fig. S2.D). From Fig. S2.D one can clearly observe a structurally different pattern at 85 °C, which according to DSC/TG corresponds to a desolvated phase and a continuous transformation into the pure α phase and a molten phase at 155 °C. These results are in complete agreement with DSC/TG.

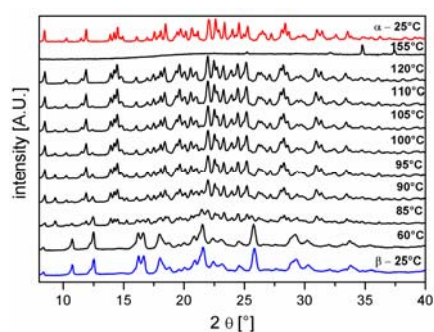


Fig. S2.D: Structural transformation of β-IMC during thermal treatment.

S3: The sample (SBA-15 and MCM-41) densities and compositions

The densities were measured with He-pycnometry and thus correspond to the mass divided by excluded volume, i.e. the volume that is inaccessible to He atoms. The mass fractions of components were determined on the basis of the first and second weight loss stages in the TG experiments.

Table S3: Sample densities and compositions

sample	ρ [g/cm ³]	φ_{SBA}	φ_{IMC}	φ_{THF}
SBA-15	2,367	1	0	0
SBA-15-IMC1	2,276	0,808	0,154	0,038
SBA-15-IMC2	2,188	0,768	0,19	0,042
SBA-15-IMC3	1,875	0,706	0,265	0,029
SBA-15-IMC4	1,785	0,628	0,3372	0,035
SBA-15-IMC5	1,675	0,5502	0,4073	0,0425
SBA-15-IMC6	1,569	0,4523	0,4984	0,04925
MCM-41	2,395	1	0	0
MCM-41-IMC1	2,110	0,826	0,156	0,0185
MCM-41-IMC2	2,101	0,803	0,1772	0,0198
MCM-41-IMC3	2,050	0,754	0,2224	0,0235
MCM-41-IMC4	1,870	0,663	0,3067	0,0303
MCM-41-IMC5	1,818	0,568	0,394	0,038
MCM-41-IMC6	1,708	0,455	0,4994	0,0461

S4: Theoretical considerations of phase transformations in spatial confinement

S4.1 Theoretical explanation of the appearance and predominance of the γ phase in progressively smaller pores.

For a review of the related thermodynamic methodology see for example⁴.

First one needs to consider that two distinct phases can be formed from the parent (desolvated) phase, the thermodynamically stable γ IMC phase and the metastable α phase, which is formed from the bulk parent phase (i.e. in absence of spatial confinement). Since γ is the stable phase and the free energy difference with respect to the parent phase (the bulk contribution to the total free energy) is, by definition, larger, the (completely) preferential formation of the α phase in absence of spatial confinement must be due to a larger free energy barrier for nucleation which, in turn, must be due to a more unfavorable surface energy contribution. In our case the phase transformation occurs in confinement conditions inside the pores, and can thus be influenced in - at least - two distinct ways. First the presence of the

pore wall may change the free energy barrier and, second, there may be specific size effects which favor the appearance of one phase over the other. One can show by means of two limiting cases that - providing the interfacial energy between the newly forming nucleus of one phase and the pore wall fulfills certain conditions - then the lowering of pore diameter may in fact cause the (otherwise unobserved) preferential formation of the γ phase. Due to the present geometry, however, the problem is far from being trivial.

The free energy of formation of a crystalline nucleus ε from a parent phase χ in contact with a surface ψ (see Fig. S4.A) can be written as the sum of volume free energy difference between the phases and changes in interfacial free energies ⁴:

$$\Delta G(N) = N(g^\varepsilon - g^\chi) + \sigma^{\varepsilon\chi}(A^{\varepsilon\chi}(N, \theta) - A^{\varepsilon\psi}(N, \theta)\cos\theta) \quad (\text{S4.1.1})$$

where $(g^\varepsilon - g^\chi) = \Delta g^{\varepsilon\chi}$ is the volume free energy difference between phases ε and χ (which does not necessarily correspond to the bulk phases), $A^{xy}(N, \theta)$ denotes the interfacial area between phases x and y as a function of the contact angle and number of molecules in the nucleus and σ^{xy} denotes the specific interfacial free energy between x and y .

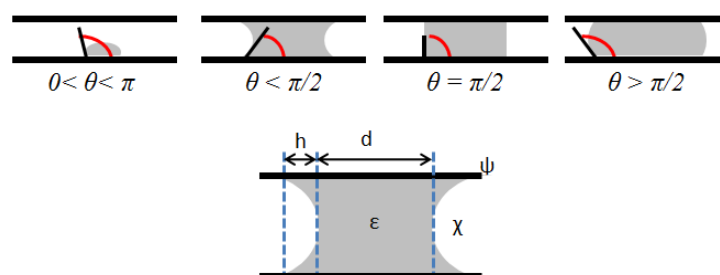


Fig. S4.A: Schematic of nucleation in the case of two limiting scenarios (small and large nucleus).

The contact angle contains the information of interactions between the three phases (ε , χ and ψ) and can be estimated using Young's equation for mechanical equilibrium of a three-phase contact:

$$\sigma^{\varepsilon\psi} = \sigma^{\varepsilon\chi} - \sigma^{\varepsilon\chi}\cos\theta \quad (\text{S4.1.2})$$

which holds for $0 \leq \theta \leq \pi$. The equation for ΔG is general and, providing the applicability of the classical nucleation theory, holds for arbitrary geometry. From there one immediately recognizes that the free energy barrier is lowered by the presence of surfaces. Specifically for the present geometry (crystalline embryo in a cylindrical pore) if assuming a spherical curvature of the ε/χ interface there are several distinct cases depicted in Fig. S4.A. For small

nuclei one can approximate the situation with the minimalistic scenario of a spherical nucleus on a flat surface. In this case the interfacial areas read

$$A^{\varepsilon X}(N, \theta) = 2\pi^{1/2}(1 - \cos\theta)(3v_1^{\varepsilon})^{2/3}(2 - 3\cos\theta + \cos^3\theta)^{-2/3}N^{2/3} \quad (\text{S4.1.3})$$

$$A^{\varepsilon\psi}(N, \theta) = \pi^{1/2}(3v_1^{\varepsilon})^{2/3}(2 - 3\cos\theta + \cos^3\theta)^{-2/3}N^{2/3} \quad (\text{S4.1.4})$$

Meanwhile, for nuclei that are large enough to extend across the pore diameter the corresponding interfacial areas are written as

$$A^{\varepsilon X}(\theta) = \begin{cases} 4\pi(1 - \cos(\pi/2 - \theta))r^2 & 0 < \theta < \pi/2 \\ 2\pi r^2 & \theta = \pi/2 \\ 4\pi(1 - \cos(\theta - \pi/2))r^2 & \pi/2 < \theta < \pi \end{cases} \quad (\text{S4.1.5})$$

$$A^{\varepsilon\psi}(\theta) = 2\pi r(d(N, \theta) + 2h(\theta)) \quad (\text{S4.1.6})$$

where

$$d(N, \theta) = \begin{cases} Nv_1^{\varepsilon}/\pi r^2 + 2(2 - 3\cos(\pi/2 - \theta) + \cos^3(\pi/2 - \theta))r/3 & 0 < \theta < \pi/2 \\ Nv_1^{\varepsilon}/\pi r^2 & \theta = \pi/2 \\ Nv_1^{\varepsilon}/\pi r^2 - 2(2 - 3\cos(\theta - \pi/2) + \cos^3(\theta - \pi/2))r/3 & \pi/2 < \theta < \pi \end{cases} \quad (\text{S4.1.7})$$

$$h(\theta) = \begin{cases} r((\sin(\pi/2 - \theta))^{-1} - ([\sin^{-2}(\pi/2 - \theta)] - 1)^{1/2}) & 0 < \theta < \pi/2 \\ 0 & \text{otherwise} \end{cases} \quad (\text{S4.1.8})$$

where v_i^{ε} denotes the volume of a molecules in phase i . Note that the expressions for both limiting scenarios are exact. For intermediate nuclei sizes the expressions become complicated if one wants to account for the actual geometry. They are in fact not crucial for what we wish to show here. The free energy barrier to nucleation is given by the condition $\partial\Delta G/\partial N=0$, in other words a nucleus will be stable if upon removal of a molecule the free energy will be increased. In case of small nuclei we get

$$\Delta G^b(N) = \frac{4\pi\sigma^{\varepsilon X^2}v_1^{\varepsilon^2}(2 - 3\cos\theta + \cos^3\theta)}{3\Delta g^{\varepsilon X}} \quad (\text{S4.1.9})$$

indicating that we must expect that both α and γ phases will be formed if

$$\frac{\Delta g^{\gamma X}\sigma^{\alpha X^2}v_1^{\alpha^2}(2 - 3\cos\theta_{\alpha} + \cos^3\theta_{\alpha})}{\Delta g^{\alpha X}\sigma^{\gamma X^2}v_1^{\gamma^2}(2 - 3\cos\theta_{\gamma} + \cos^3\theta_{\gamma})} \sim 1 \quad (\text{S4.1.10})$$

and the γ phase will be formed predominantly if

$$\frac{\Delta g^{\gamma\chi} \sigma^{\alpha\chi} v_1^{\alpha^2} (2 - 3\cos\theta_\alpha + \cos^2\theta_\alpha)}{\Delta g^{\alpha\chi} \sigma^{\gamma\chi} v_1^{\gamma^2} (2 - 3\cos\theta_\gamma + \cos^2\theta_\gamma)} \gg 1 \quad (\text{S4.1.11})$$

The γ phase is thermodynamically stable ($|\Delta g^{\alpha\chi}| < |\Delta g^{\gamma\chi}|$) thus the transformation in the bulk is directed towards α phase because $|\sigma^{\alpha\chi}| \ll |\sigma^{\gamma\chi}|$. The presence of the pore surface will effectively lower the interfacial energy contribution for all nucleus sizes and will thus favour formation of the γ phase. The larger the interfacial contact area the more γ phase will be formed.

In case of large nuclei, the free energy barrier does not depend on N . In this case a nucleus will be stable if $\partial \Delta G / \partial N \leq 0$ or explicitly the pore radius satisfies the inequality

$$r \leq 2\sigma^{\alpha\chi} v_1^{\alpha^2} \cos\theta / \Delta g^{\alpha\chi} \quad (\text{S4.1.12})$$

Thus the larger the contact with the surface or in other words, the smaller the pore size, the greater is the probability that the nucleus will be stable (which holds for both phases). Moreover the smaller the pore size, the larger will be the contact area and thus smaller free energy barrier for γ phase formation.

Note that the limit of small nuclei represents only a lower bound, that is, it is in a sense the most conservative bound (the nucleus/wall contact area relative to the nucleus solution area at given contact angle would always be larger in cases where the nucleus size is between both limits considered here). If one would attempt to write down equations for scenarios that interpolate between both limiting scenarios, the critical difference in contact angles, expressed as $\theta_\alpha/\theta_\gamma$, which already leads to co-existence of phases α and γ which would result in the predominance of the γ phase in those interpolating scenarios would always be lower than the one prescribed by the lower bound. This explains the observation, that the γ phase is formed predominantly in smaller pores.

S4.B: Theoretical explanation of the pore size dependent initial phase formation

Heterogeneous nucleation theory can also be used to explain the differences in the experimentally observed initial-phase evolution upon increasing loading. One again starts from Eq. S4.1.1 with the difference that the parent phase χ now represents the supersaturated solution and also that $\Delta g^{\alpha\chi}$ is composition-dependent. More specific $\Delta g^{\alpha\chi}$ is proportional to the logarithm of the superaturation, $-k_b \ln S$, where the superaturation is defined as the ratio of the activity of the solute with its equilibrium bulk activity, $S \equiv a/a_{eq}$. Since THF is continuously

removed by drying (i.e. THF molecules evaporate from the solution inside the pores) the supersaturation also increases continuously. The height of the free energy barrier, of course, corresponds to the the extremum of free energy as a function of nucleus size, $\partial AG/\partial N = 0$. In the limit of a small nucleus the free energy barrier has a $1/\ln S$ dependence. In the limit of a large nucleus the critical pore size also has a $1/\ln S$ dependence. Regarding the dimensions of pore diameters under consideration and typical values of interfacial energies one can expect that the scenario of a nucleus extending throughout the entire pore diameter is far more likely. Namely, the supersaturation must have an upper bound (at a certain composition the remaining IMC and THF molecules will simply adsorb to the wall surface to lower their free energy), and it is not likely that a small nucleus will be stable before the upper bound is reached. In the latter case, the reorganization of adsorbed molecules into a crystalline nucleus will be kinetically severely hindered. One can reason that the decision whether a situation, where the remaining molecules simply adsorb to the surface because they are too few to form a stable nucleus, is reached before the supersaturation dependent free energy barrier to nucleation can be surmounted, will depend on the initial concentration. Namely it is not expected that a single nucleation event will proceed inside a cylindrical pore, which in turn limits the number of molecules which can participate in nucleation attempts. From equation S4.1.12 one gets using $\Delta g^{ex} = -k_b \ln S$ for the critical supersaturation $S_c = \exp(-2\sigma^{ex} v_l^e \cos\theta / k_b r_{pore})$, wherefrom it follows that lower supersaturations are necessary in smaller pores. This explains the observation that a crystalline phase is formed in small pores already at low loadings.

S5: Nitrogen sorption isotherms and pore size distributions

All the nitrogen adsorption-desorption isotherms are found to be of type IV sorption isotherms according to the IUPAC classification and exhibit well-defined H1 hysteresis loops, which are typical for SBA-15 and MCM-41 silicates. The presence of H1 hysteresis type confirms that they have open-ended cylindrical mesopores. Both isotherms have a hysteresis loops with sharp adsorption-desorption branches, which indicates a narrow pore size distribution in both silicates (Fig. S5.A).

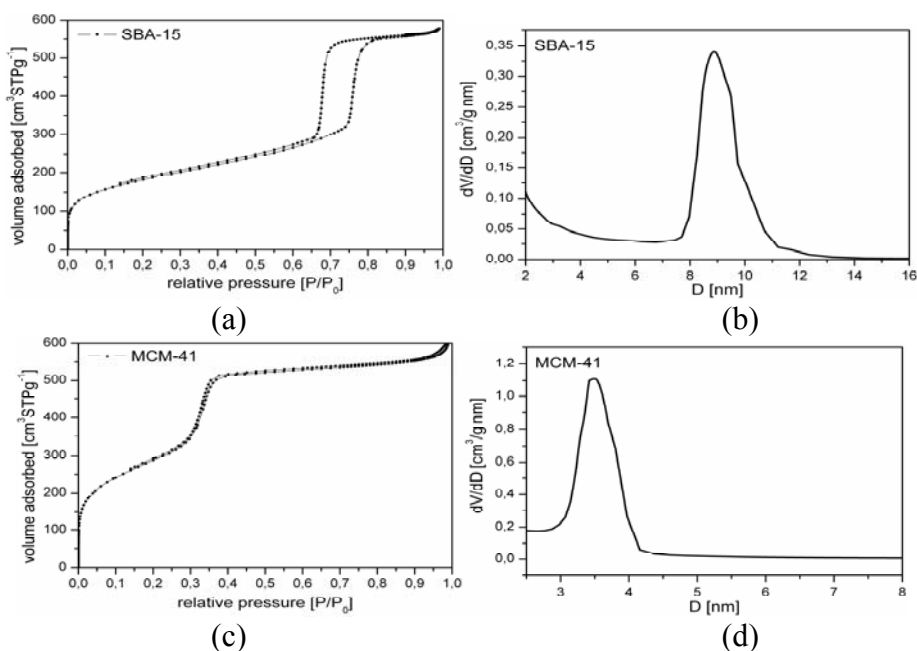


Fig. S5.A: Nitrogen sorption isotherms (left; (a) and (c)) and pore size distributions (right; (b) and (d)) of SBA-15 and MCM-41.

Table S5.B: Structural properties of SBA-15 and MCM-41 samples

Sample	S_{BET} (m ² /g)	V_t (cm ³ /g)	V_{mi} (cm ³ /g)	d_{me} (nm)
SBA-15	625	0.893	0.050	8.9
MCM-41	1045	0.929	/	3.5

Abbreviations: BET specific surface area (S_{BET}): Brunauer-Emmett-Teller (BET) equation; total pore volume (V_t): single-point volume at $p/p_0 = 0.989$; micropore volume (V_{mi}): t-plot method; mesopore diameter (d_{me}): at the maximum of the BJH pore size distribution

X-ray diffraction and nitrogen adsorption-desorption isotherms measurements were performed for each loading concentration in order to calculate the pore size distributions.

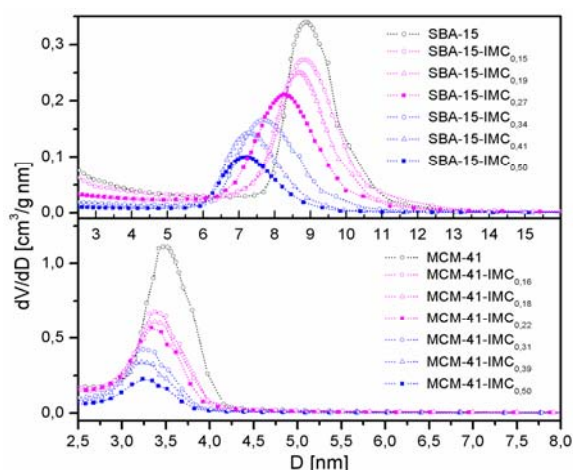


Fig. S5.C: Pore size distributions of prepared samples: (upper panel) SBA-15 derived samples (bottom panel) MCM-41 derived samples.

As observed in Fig. S5.C the pore size and pore volume of SBA-15 derived decrease significantly upon increasing the loading fraction. The decrease of pore diameter indicates that, most likely, an incomplete ad-layer is formed. In the case of MCM-41 derived samples the pore volume also decreases significantly upon increasing loading, whereas the pore size does not change appreciably. The latter indicates that here the formation of an ad-layer does not occur.

S6: Calculation of densities of confined phases and maximal surface fraction that can be covered by IMC and THF molecules

S6.1 Sample densities

If assuming that the density (the mass divided by volume that is inaccessible to He atoms) of the silicate matrix does not change upon drug loading (which is a very reasonable assumption as SiO₂ is insoluble in THF and does not react with it either) the density of the confined phase (IMC+THF) may be calculated from the density of the pure matrix and the measured total density. After some elementary algebraic manipulation it can be written as:

$$\rho = \frac{\rho_T \rho_m (1 - \varphi_m)}{\rho_m - \rho_T \varphi_m} \quad (\text{S6.1.1})$$

where ρ_T represents the measured density of the sample, ρ_m is the density of pure matrix, and φ_m is the mass fraction of the matrix. In an infinitely diluted phase (i.e. all molecules are completely isolated) the maximum possible density, which can be measured by He-pycnometry (the excluded volume density of isolated molecules), corresponds to the Connolly volume of the phase with a certain composition. Using the mass fractions of IMC and THF, obtained from DTA-TG measurements, one can calculate this maximal density, which we call here Connolly density, as:

$$\rho_C = \left\{ \left(\frac{1 - \varphi_{IMC}^x}{M_{THF}} v_{THF}^{Con} + \frac{\varphi_{IMC}^x}{M_{IMC}} v_{IMC}^{Con} \right) N_A \right\}^{-1} \quad (\text{S6.1.2})$$

where φ_{IMC}^x stands for the relative mass fraction of IMC in the mixture with THF while v_{THF}^{Con} and v_{IMC}^{Con} represent the Connolly volumes of the THF and IMC molecules when measured with a He atom with van der Waals radius 2.11 Å, M_{THF} and M_{IMC} denote molecular masses and N_A stands for Avogadro's number. The Connolly volumes were estimated using molecular conformations obtained by vacuum energy minimization on the molecular mechanics MM2 level.

S6.2 Maximal surface coverage

A very naive explanation of the evolution of the confined phase upon increasing fraction was given by Mellaerts *et al.*⁵ in terms of the exceeded capacity for monolayer formation. In this spirit the structural transition from a molecular dispersion to a crystalline phase occurs when the matrix surface cannot accommodate all confined molecules in the form of a monolayer anymore. Such adsorption of all drug molecules in the form of a monolayer is, from a thermodynamical point of view, impossible at all concentrations due to an infeasible entropic barrier. Nevertheless, the calculation of the fraction of accessible matrix area covered by confined molecules might offer some additional insight into the evolution of the confined phase upon increasing fraction. To be able to do so one must unavoidably estimate the area of molecules which is to be in contact with the surface which, in turn, cannot be *ad-hoc* unambiguously defined. Furthermore, due to the geometry of pore surfaces it is not expected that the molecules in the monolayer will assemble in a close packing regime, thus estimates analogous to Connolly volumes would not be meaningful. As a first approximation, it seems most reasonable to estimate the contact areas from the volumes that are occupied by the molecules in crystalline phases, i.e. $(v_i^{cryst})^{2/3}$. In this case the fraction of matrix surface area covered by the molecules in the confined phase (IMC and THF) - if they formed a monolayer - can be estimated as

$$\kappa_S = \frac{\left(\frac{\varphi_{IMC}^{cryst} v_{IMC}^{cryst} N_A}{M_{IMC}} + \frac{\varphi_{THF}^{cryst} v_{THF}^{cryst} N_A}{M_{THF}} \right)}{\varphi_{m,m}} \quad (S6.1.3)$$

where s_M and $\varphi_{M\#}$ stand for the specific surface area and mass fraction of the matrix. κ_S is calculated by taking $v_{IMC}^{cryst} = 417 \text{ \AA}^3$ from ref.² (the smallest volume of the IMC molecule observed in a crystalline phase) and $v_{THF}^{cryst} = 101 \text{ \AA}^3$ from ref.⁶

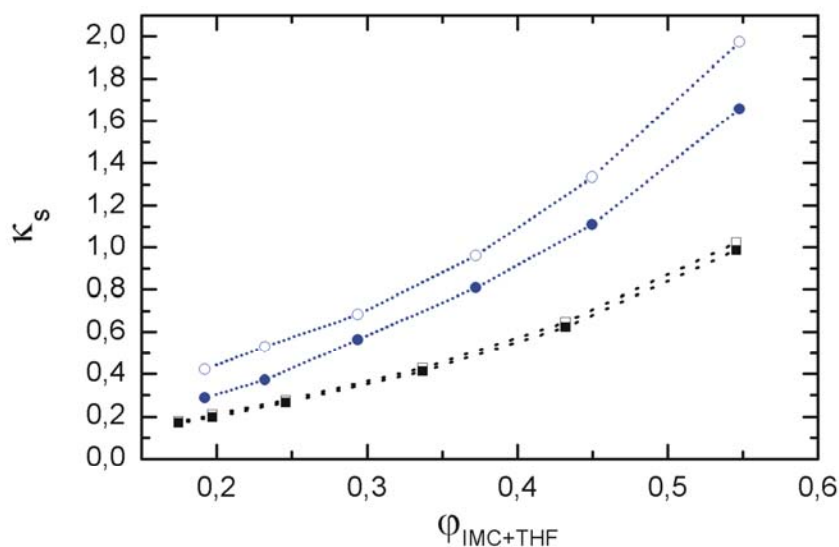


Fig. S6A: Fraction of silicate matrix surface covered if depositing all molecules of the confined phase with given mass fraction and composition in the form of a monolayer based on the computational approach explained in the text. Blue symbols correspond to SBA-15 derived samples and black ones to MCM-41 derived samples. Full symbols represent coverage by IMC molecules only and empty symbols denote the coverage by THF and IMC molecules.

S7: Structure, pore size and wall thickness as determined by XRPD and Transmission electron microscopy (TEM)

The structure of calcined and with IMC loaded SBA-15 and MCM-41 silicates was investigated by XRPD. XRPD patterns of both calcined and loaded samples show three well-resolved maxima, which are assigned to the (100), (110) and (200) reflections of a hexagonal well ordered structures (p6mm space group). The changes in the SBA-15+IMC and MCM-41+IMC diffraction patterns might be caused by pore loading with IMC. However, it should be pointed out that after loading procedure the XRPD of both loaded silicates showed no loss of structural order of the porous network.

TEM images clearly depict hexagonal arrangements of the pore system and the uniformity of the cylindrical pores. The average pore diameter of the silicates is in good agreement with the one calculated from the XRPD patterns (see below) and N_2 sorption measurements.

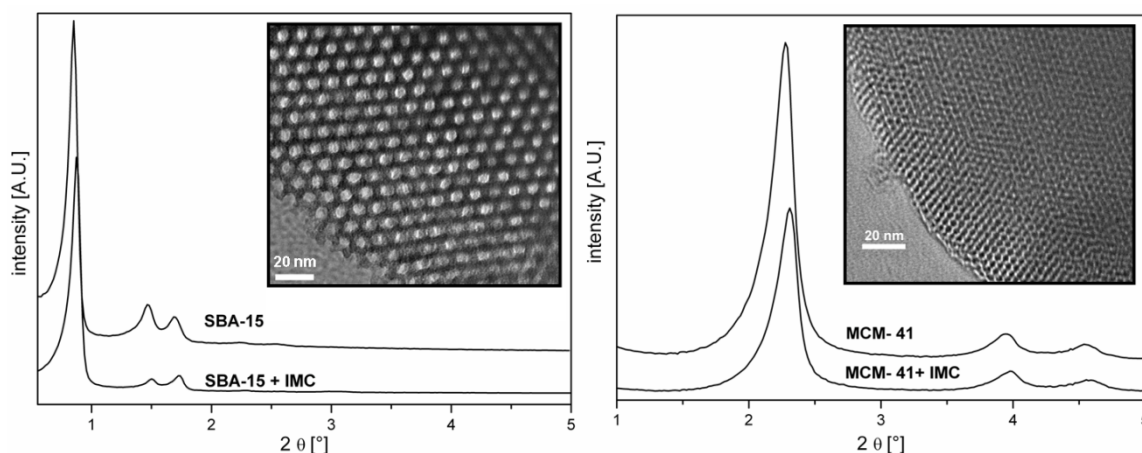


Fig. S7.A: XRPD patterns of pure and loaded SBA-15 ($\phi_{\text{IMC}}=0,5$) (left) and MCM-41 ($\phi_{\text{IMC}}=0,5$) (right) samples. The inset represents corresponding TEM images of pure calcined samples.

The (100) d -spacing from the XRPD pattern was calculated to obtain the a -parameter (denoted as a_0), which is the mesopore center-to-center distance ($a_0 = 2d_{100}/3^{1/2}$). The calculated a_0 value was combined with adsorption results to assess the thickness of mesopore wall ($h_w = a_0 - d_{me}$, where h_w is wall thickness and d_{me} is the average mesopore size determined from N_2 analysis).

Table S7.B: Powder X-Ray diffraction patterns of SBA-15 and MCM-41 samples

Sample	d_{100} (nm)	a_0 (nm)	d_{me} (nm)	h_w (nm)
SBA-15	10.35	11.95	8.9	3.05
SBA15-IMC6	10.09	11.65	7.2	4.45 (IMC+wall)
MCM-41	3.87	4.47	3.5	0.97
MCM41-IMC6	3.82	4.41	3.2	1.21 (IMC+wall)

Unit-cell size (a_0): calculated from the d_{100} data (the d_{100} numbers represent the d -spacing corresponding to the main (100) XRD peak) using the formula $a_0 = 2d_{100}/3^{1/2}$; pore wall thickness (h_w): calculated using the formula $h_w = a_0 - d_{me}$; mesopore diameter.

As seen in Table S7.B, h_w increases significantly upon loading in the case of SBA-15, which indicates that a (probably incomplete) molecular layer of IMC or THF molecules is (also) formed. The thickness of the layer (0.7 nm) is in the range of the size of an IMC molecule. In case of MCM-41, h_w increases only slightly and the thickness of the ad-layer would correspond to 0.1 nm which is well below the IMC molecular size. This indicates that in the case of MCM-41 no molecular layer is formed. These results are in complete agreement with those from nitrogen sorption analysis.

S8: Solid-state NMR spectroscopy

S8.1 Bulk indomethacin phases and the IMC/THF ratio in the beta form

Solid-state MAS NMR spectroscopy clearly distinguishes between the three forms of indomethacin in the bulk (Fig. S8.A). In the spectra of carbon nuclei individual lines are narrow and well resolved. Without a demanding analysis and just by counting the signals in the spectra, one can also see that γ gamma form has one molecule of indomethacin in the asymmetric unit, α form has three molecules of indomethacin in the asymmetric unit, and β form has two molecules of indomethacin in the asymmetric unit. In addition to signals of indomethacin, in the spectrum of β form we can also distinguish signals that belong to molecules of THF. Estimation of peak areas suggests that in this solvate the asymmetric unit comprises one THF molecule. Note that although cross-polarization measurements generally do not provide quantitative information, comparison of signal intensities for $-\text{CH}_2-$ groups of indomethacin and for $-\text{CH}_2-$ groups of THF can yield a relatively reliable estimation. The above ratio of one THF molecule per two indomethacin molecules is also supported by proton MAS NMR spectroscopy.

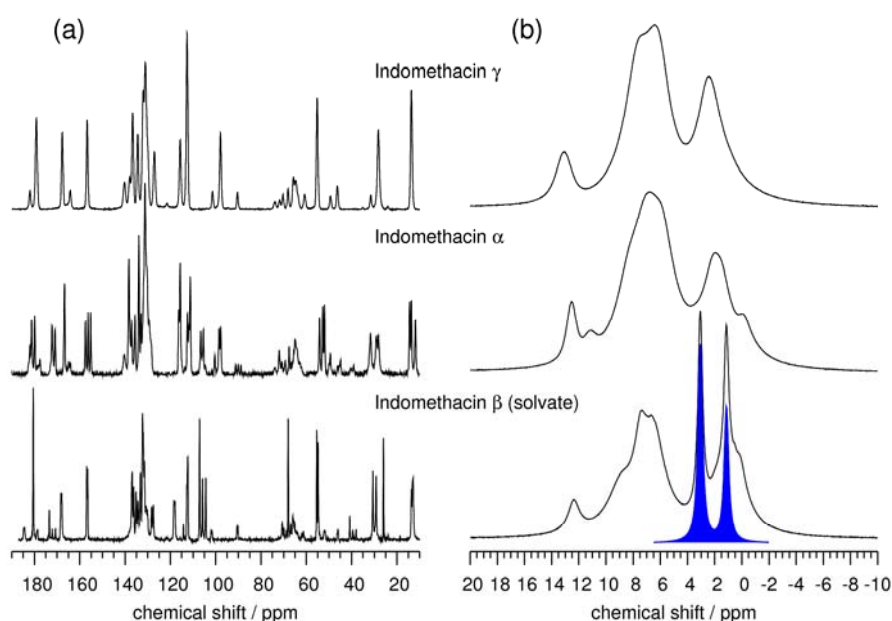


Fig. S8.A: ^1H - ^{13}C CPMAS (a) and ^1H MAS NMR spectra (b) of bulk indomethacin phases. In case of IMC β the area under the two ^1H signals that belong to THF (indicated in blue) compared to the area under the remaining ^1H spectrum yields an IMC/THF ratio equal to 2.0.

S8.2 Indomethacin confined within the mesopores of SBA-15 and MCM-41

Compared to those of α , β and γ polymorphs in the bulk, the NMR signals in carbon spectra of SBA15-IMC6 ($\phi_{\text{IMC}}=0.5$) and MCM41-IMC6 ($\phi_{\text{IMC}}=0.5$) samples are drastically broader (Fig. S8.B). Obviously, carbon nuclei of indomethacin molecules within the pores of SBA-15 and MCM-41 experience a distribution of environments, which leads to a distribution of isotropic chemical shifts. Although DSC measurements in both samples detected phase transitions typical for crystalline materials, small dimensions of the 'crystallites' and the corresponding large surface contribution still lead to broad lines, which are otherwise characteristics of amorphous materials. Note that the spectra of as-prepared SBA15-IMC6 and MCM41-IMC6 samples are almost identical, which suggests that at this stage the samples probably do not comprise different amounts of α , β and γ phases. The differences observed by DSC measurements are thus indeed most probably induced by effects of confinement on the phase transformations.

When SBA15-IMC6 ($\phi_{\text{IMC}}=0.5$) was heated to 130 °C (Fig. S8.B), weak narrow signals appeared in the carbon NMR spectrum in addition to broad signals discussed above. Chemical shifts of the narrow peaks suggest that they belong to indomethacin in α form. Their appearance not only shows that phase transition to α form has taken place but also indicates that upon thermal treatment part of indomethacin nanoparticles grows to sufficiently large and well-ordered crystallites that within them the distribution of environments and the distribution of chemical shifts becomes narrow. Such transition to γ form is not observed in the case of MCM41-IMC6 ($\phi_{\text{IMC}}=0.5$), which can probably be ascribed to the fact that IMC particles within the narrower pores of MCM-41 cannot grow as large as the particles within the pores of SBA-15.

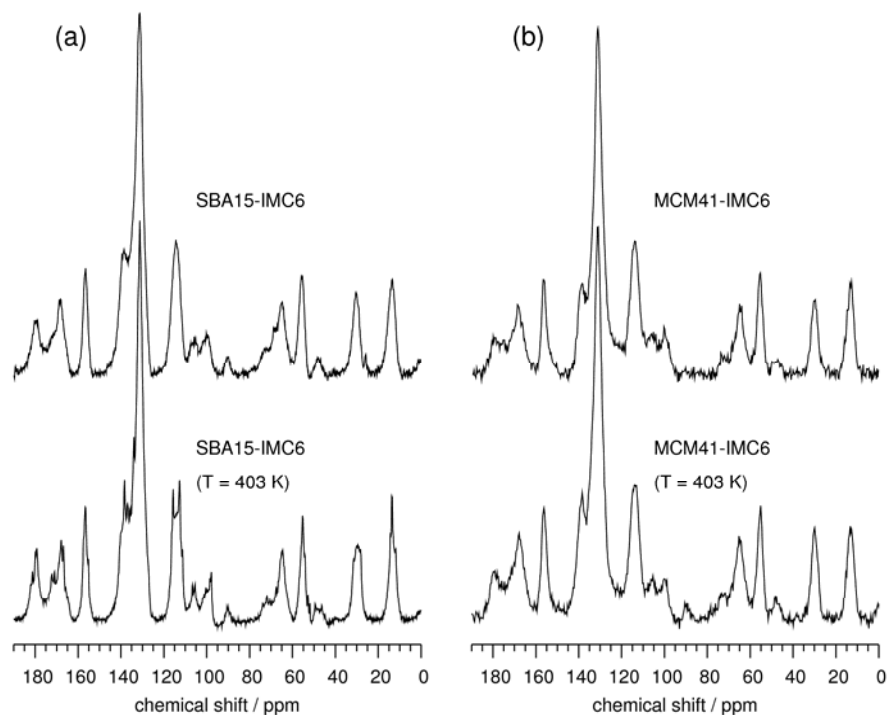


Fig. S8.B: ^1H - ^{13}C CPMAS NMR spectra of loaded SBA-15 ($\phi_{\text{IMC}}=0.5$) (left) and MCM-41 ($\phi_{\text{IMC}}=0.5$) (right) samples (as prepared and heated to 130 °C).

At first sight, the spectra of different SBA15-IMC samples are very similar (Fig. S8.C). In the spectrum of SBA15-IMC1 ($\phi_{\text{IMC}}=0.15$) two sharp signals belonging to THF molecules are detected. The isotropic chemical shifts of these signals are not the same as the isotropic chemical shifts of signals of THF molecules within bulk crystalline β . They indicate the presence of the excess THF molecules, which explain why a low $n_{\text{IMC}}/n_{\text{THF}}$ ratio was detected in SBA15-IMC1. In the spectra of SBA15-IMC3 ($\phi_{\text{IMC}}=0.27$) and SBA15-IMC6 ($\phi_{\text{IMC}}=0.50$) sharp THF peaks become negligible.

The most important differences between carbon spectra of SBA15-IMC1, SBA15-IMC3, and SBA15-IMC6 are in the signals at around 180 ppm and around 170 ppm, i.e. in the signals of carboxyl and carbonyl groups, respectively. Since these two groups can participate in hydrogen bonds, the differences in the spectrum of SBA15-IMC1 suggest that in this sample hydrogen bonds are different than in samples SBA15-IMC3 and SBA15-IMC6, or that the bonds are not present at all. This nicely agrees with the above conclusion that indomethacin is incorporated into SBA15-IMC1 in the form of a molecular dispersion, whereas within SBA15-IMC3 and SBA15-IMC6 it forms crystalline particles. A careful analysis of proton spectra using decomposition into individual contributions shows that the width of the main signal at approximately 6.8 ppm changes from 2.2 ppm (fwhm) for sample SBA15-IMC1 to

2.8 ppm for sample SBA15-IMC6. Since linewidths of proton spectra are mostly determined by the strength of the (residual) homonuclear proton-proton dipolar interaction, the increasing linewidth suggests that this interaction is getting stronger and stronger. This further implies that the network of protons is getting more and more rigid or more and more dense, which could be a consequence of concentrating and assembling of indomethacin molecules or clusters into nanoparticles.

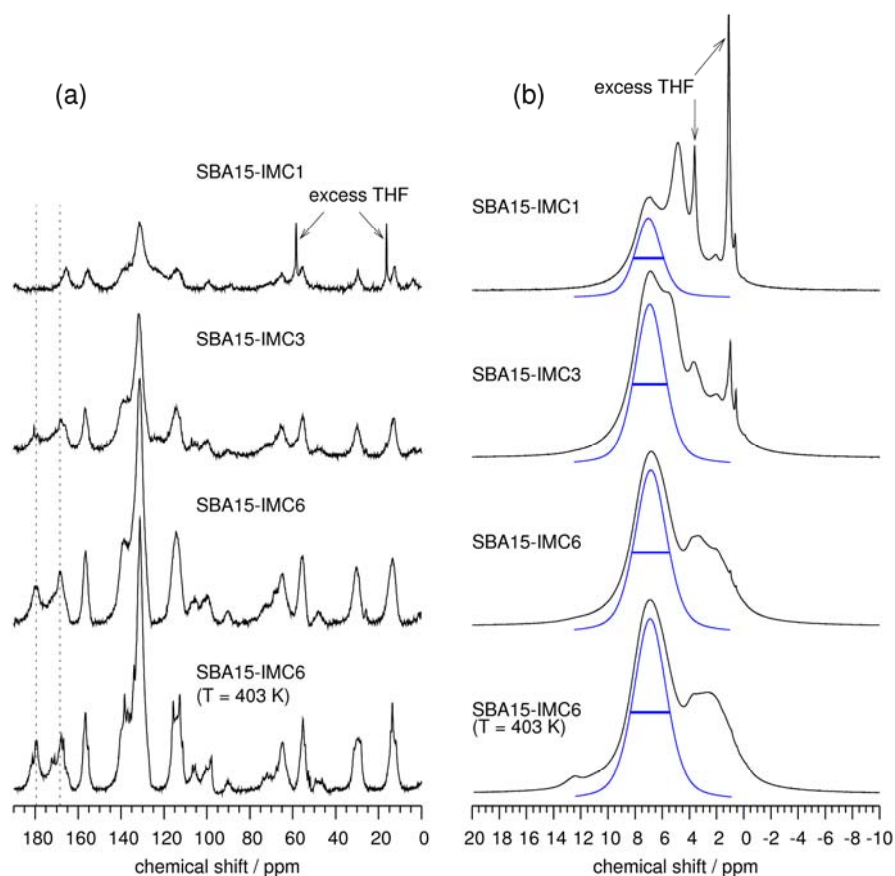


Fig. S8.C: ^1H - ^{13}C CPMAS (a) and ^1H MAS NMR spectra (b) of loaded SBA-15 based samples. Horizontal blue lines indicate the width of the main proton signal resonating at 6.8 ppm.

Additional References :

- 1 T. J. Kistenmacher and R. E. March, *J. Am. Chem. Soc.*, 1972, **94**, 1340.
- 2 X. Chen, K. R. Morris, U. J. Griesser, S. R. Byrn and J. G. Stowell, *J. Am. Chem. Soc.*, 2002, **124**, 15012.
- 3 N. Hamdi, Y. Feutelais, N. Yagoubi, D. de Girolamo and B. Legendre, *J. Therm. Anal. Calorim.*, 2004, **76**, 985–1001.

4 J. W. Christian, Elsevier Science Ltd, Oxford UK 2002; C. Alba-Simionesco, B. Coasne, G. Dosseh1, G. Dudziak, K. E. Gubbins, R. Radhakrishnan and M. Sliwinska-Bartkowiak, *J. Phys.: Condens. Matter*, 2006, **18**, R15.

5 R. Mellaerts, C. A. Aerts, J. Van Humbeeck, P. Augustijns, G. Van den Mooter and J. A. Martens, *Chem. Commun.*, 2007, **13**, 1375.

6 P. Luger, J. Buschmann and J. Twist, *Angew. Chem. Int. Ed.*, 1983, **22**, 410.